Vat Photopolymerization of Poly(styrene-*b*-isoprene-*b*-styrene) Triblock Copolymers

Ren H. Bean[1], Garvit Nayyar[1], Margaret K. Brown[3], Jianheng Wen[1], Yiqun Fu[2], Karen I. Winey[3], Christopher B. Williams[2], and Timothy E. Long[1*]

[1]School of Molecular Sciences & Biodesign Center for Sustainable Macromolecular Materials & Manufacturing (SM3), Arizona State University, Tempe, AZ 85281
[2]Department of Mechanical Engineering, Macromolecules Innovation Institute, Virginia Tech, Blacksburg, VA 24061
[3]Department of Materials Science and Engineering, University of Pennsylvania, Philadelphia, PA 19104

*To whom correspondence should be addressed. Email: telong@asu.edu. TEL: (480) 965-9539

Abstract:

Vat photopolymerization (VPP) additive manufacturing (AM) produces complex geometries with micron-scale resolution and smooth surface finish from a wide range of photocrosslinkable polymeric precursors. However, mass transport limitations typically constrain VPP amenable precursors to viscosities less than 10 Pa·s. Reactive oligomers and monomers comprise the majority of VPP polymeric precursors, which result in highly crosslinked and brittle 3D objects upon printing. This work describes colloidal high molecular weight ABA triblock copolymers, or latex, as a feedstock for aqueous photoreactive compositions to enable AM of thermoplastic elastomers (TPE). Photorheological analysis determined 15 wt. % aqueous reactive monomers and oligomers generated a structural scaffold that achieved sufficiently high modulus to maintain feature fidelity for iterative layer formation. Subsequent thermal post-processing removed water and promoted polymeric particle coalescence throughout the scaffold resulting in an interpenetrating network (IPN) that exhibited an isotropic dimensional shrinkage of 25%. Small-angle X-ray scattering (SAXS) confirmed microphase-separated morphologies typical of triblock copolymers, revealing a characteristic length scale of 30 nm. Using commercially available VPP printers, ABA triblock copolymer poly(styrene-*b*-isoprene-*b*-styrene) latex yielded printed elastomers with precise feature fidelity and tensile extensibility exceeding 800%.

Keywords: Block copolymer, Latex, Photopolymerization, SIS, 3D Printing

1.0 Introduction:

Vat photopolymerization (VPP) is a transformative additive manufacturing (AM) technique, which enables the fabrication of precise and intricate geometries unachievable through conventional polymer processing methods. However, the printed objects typically consist of highly crosslinked brittle polymeric networks, which significantly limits VPP's use in functional applications. Traditionally, VPP employs a layer-by-layer approach delivering ultraviolet (UV) light to initiate free radical photocuring of liquid precursors. The resulting three-dimensional (3D) objects exhibit excellent micron-scale resolution, isotropic mechanical properties, and a smoother surface finish than those fabricated using alternative AM methods. [1, 2] Typical VPP amenable polymeric resins maintain viscosities less than 10 Pa·s, which dictates maximum processable molecular weight.[3-6] The primary factor is mass diffusion limitations during recoating processes between the photocuring of each layer. Furthermore, successful VPP demands each layer achieve sufficient modulus, typically in the range of 10^4-10^5 Pa, to maintain feature fidelity.[7-10] These criteria collectively direct VPP compositions toward low molecular weight precursors, which result in high crosslink densities and imperfect networks that provide suitable modulus but inferior elasticity. Copolymerization during VPP printing provides linear polymers that reduce crosslink density but fails to attain sufficient molecular weight due to oxygen inhibition.[11] Thus, current VPP compositions for providing highly elastic objects remain limited.

Block copolymers represent a versatile class of polymeric materials, which are comprised of distinct polymeric segments covalently bonded together. ABA triblock copolymer nomenclature is well-established to define the sequence of the copolymer, and ABA triblock copolymers, often termed thermoplastic elastomers, are comprised of three blocks consisting of two distinct chemical compositions (e.g., poly(styrene-b-isoprene-b-styrene)). The external A blocks are polystyrene, and the central B block is polyisoprene. Their unique architecture enables varied combinations of chemically dissimilar polymers providing versatile structure-property relationships within a single molecule. Commonly, block copolymers find applications in the automotive[12-14], packaging [15, 16], medical [17-21], and electronics industries[22-24], where their ability to self-assemble into well-defined nanoscale structures is advantageous. For example, in the automotive industry, block copolymers are employed as elastomers, leveraging their hard and soft domains to provide strength and elasticity to automotive and sealant technologies.[25, 26] However, incorporating block copolymers into AM, particularly VPP, poses significant challenges. Macrophase separation of the block copolymers in a multiphase composition interferes with the printing process resulting in diminished resolution and structural integrity.[27, 28] Additionally, incompatibility within chemically dissimilar VPP compositions drives unfavorable and uncontrolled phase separation complicating the achievement of uniform mechanical properties. These challenges have, until now, limited the exploration of 3D printing block copolymers and thus the ability to leverage their distinct advantages.

The versatility of block copolymers has led to their application in diverse 3D printing techniques such as polymer powder bed fusion (PBF), fused filament fabrication (FFF), direct ink write (DIW), and VPP, facilitating the fabrication of complex structures with tailored mechanical and thermal properties. Among these, DIW and VPP are recognized for compositional diversity and superior resolution, respectively. For example, *Banerjee et al*. leveraged thermoplastic elastomer (TPE) ABA triblock copolymer poly(styrene-*b*-isoprene-*b*-styrene) (SIS) in toluene to provide extrusion 3D printed elastomers achieving high elongation; however, the fabricated object complexity was limited, and the use of organic solvents limits adaptation.[29] *Bates et al.* developed DIW pastes for the fabrication of super-soft elastomers leveraging bottlebrush copolymers, which self-assemble into well-ordered body-centered cubic (BCC) sphere phases.[30] Block copolymer side-chain length enabled control over microphase separation length scale. Additionally, stress-induced structural reversibility between a BCC lattice and disordered micelles enabled a sharp modulus transition, which facilitated printability; however, the implementation of DIW resulted in limited geometric complexity and poor resolution. Boyer *et al.* leveraged polymerization-induced microphase separation (PIMS), which was originally developed by Seo and Hillmyer,[31] to provide a photopolymerizable composition for implementation with rapid and commercially available VPP systems.[27, 28] Varying the chain length of the macro chain transfer agent (macroCTA) and block copolymer dictated domain size and domain spacing, respectively. Furthermore, the domain size followed predictable scaling behavior enabling predetermined nanostructures while leveraging VPP systems to provide geometric complexity. However, the application of PIMS encounters intrinsic limitations due to its reliance on the Flory Huggins chi (χ) parameter to drive phase separation at higher degrees of polymerization (N).[32, 33] The employment of reversible addition fragmentation chain transfer (RAFT) polymerization restricts monomer selection to acrylics. This limitation not only narrows the range of accessible polymers but also tends to yield polymers with low molecular weights compared to those synthesized through alternative methods. Additionally, this methodology's inherent exclusion of dienes-based elastomers, such as cis-1,4-polyisoprene, is frequently utilized for its elastomeric properties further limiting the exploration of structure-property relationships crucial for optimized 3D printing of nanoscale phase separated materials.

Contributing to the emerging focus on 3D printing block copolymers, *Long et al.* introduced a novel platform for vat photopolymerization of high molecular weight polymers.[34, 35] The approach utilized colloidal polymers, or latexes, to decouple the dependency of molecular weight on viscosity. Sequestering polymer chains to a discrete phase limited intermolecular interactions and provided low-viscosity feedstocks for VPP and UV-assisted DIW. The addition of water-soluble photocrosslinkable reactive monomers and oligomers provided the ability to generate a supporting scaffold upon UV irradiation to form a hydrogel green body, which effectively defines the part geometry. Subsequent thermal annealing removed water and drove polymer particle coalescence throughout the photogenerated scaffold resulting in 3D printed semi-interpenetrating network (sIPN) that leverages the desirable entanglements of high molecular weight polymers. This resulted in precisely shaped styrene-butadiene rubber (SBR) elastomers, which exhibited elongations exceeding 500%; however, VPP of these compositions required a specifically designed 3D printer, which corrected for polymer particle-induced light scattering.[34] Nonetheless, this technique demonstrated a novel platform for 3D printing high molecular weight polymers lending promising opportunities to enable VPP to fabricate elastomers with high molecular weights.

Herein, ABA triblock copolymers coupled with advanced latex VPP printing techniques is reported. Crucial parameters include latex stability, resolution driven by colloidal light scattering, homogeneous morphology in the 3D printed object, and scalability. This manuscript addresses each of these challenges to demonstrate the ability to 3D print high molecular weight

ABA triblock copolymers from water. Additionally, geometric complexity is expected from VPP, generating green bodies with a plateau modulus below traditional photoreactive resins. This scaffold further enables the 3D printing of elastomers providing a scaffold with high molecular weight between crosslinks (M_c), which is conducive to elastomer performance and ensuring proper phase separation of the embedded SIS copolymer. This work represents the first example of VPP of ABA triblock copolymer elastomers, thus enabling VPP to create complex geometries with excellent resolution and mechanical performance. Furthermore, this work demonstrates the successful VPP of a composition capable of forming precise nanostructures co-continuous within a covalent network.

2.0 Experimental:

2.1. Materials

Poly(styrene-*b*-isoprene-*b*-styrene) (SIS) rubber latex (IR2GL1) was generously provided by Cariflex, Inc. The latex had a solids content of 65 wt. %, particle diameter range of 600-900 nm, and viscosity of 150 cps as provided by the manufacturer. SEC analysis determined the SIS ABA triblock copolymer M_w of 199,000 g/mol, M_n of 140,000 g/mol, and a Đ of 1.42 (**Figure S1**). ^{1}H NMR spectroscopic analysis of the SIS triblock copolymer determined an polyisoprene content of 89 wt. % with a 1.9: 1.0 cis:trans molar ratio and a 3,4-addition of 7 mol % (**Figure S2**). 1-vinyl-2-pyrrolidinone (NVP) was purchased from TCI America. Surfactant sodium dodecyl sulfate (SDS) and poly(ethylene glycol) diacrylate (PEGDA, 575 g/mol) were purchased from Sigma Aldrich. Lithium acylphosphinate (LAP) photoinitiator was synthesized as described in previous literature.[35]

2.2. Photocurable Latex Preparation

As a standard example (15 wt. % scaffold, 5:1 NVP:PEGDA), 3.13 mL of water maintained a latex solids content of 40 wt. %. LAP (9.7 mg, 0.1 wt. %), SDS (97 mg, 1 wt. %), NVP (1.25 g, 12.5 wt. %), and PEGDA (0.25 g, 2.5 wt. %) were added to the water and dissolved with vortex mixing. The monomer/photoinitiator/surfactant solution was subsequently added dropwise to 5 g of latex stirring rapidly in a separate 20 mL vial. The resulting photocurable latex was vortexed for 30 s to ensure complete mixing.

2.3. Analytical Methods

Dynamic light scattering (DLS) measurements were conducted at 25 °C with a Malvern Zetasizer Pro Red, reporting intensity distributions. DLS samples were prepared with SIS and SIS compositions diluted to 1 wt. % solids with deionized water to minimize particle-particle interactions. Photorheological experiments were performed on a TA instruments Discovery Series HR-3 equipped with a Smart Swap™ UV assembly with 20 mm aluminum upper plate, 20 mm acrylic lower plate, and an Omnicure S2000 high-pressure mercury light source (320-500 nm filter). UV intensity was measured with a Silverline radiometer and 20 mm sensor attachment for the acrylic parallel plate. Data was collected with 500 μm gap, 0.1% strain, and 1 Hz frequency. UV radiation was applied for 15 s after a 30 s delay with an intensity of 60 mW/cm^2. An axial force of 0 N with 1 N tolerance was set to ensure proper contact throughout the test. Samples were analyzed under air without an inert gas purge. Triplicate data was acquired to ensure the reproducibility of the employed technique. Crossover moduli (G'/G") values were determined using the dedicated feature integrated in TA instruments TRIOs software. Plateau storage moduli values were determined using the last 20 s of the G' curve. Dynamic mechanical analysis (DMA) was performed on a TA Instruments Q800 Dynamic Mechanical Analyzer in tension mode at 0.1% strain, 1 Hz, with a 3 °C/min heating rate from -100 to 150 °C. Glass transition temperatures (T_g) were taken from maxima of the tan δ unless otherwise indicated. Tensile experiments were performed on an Instron 68TM-5 with a 5 kN load cell tensile tester at a strain rate of 5 mm/min at 25 °C. Tests were conducted on die-cut cast films and 3D printed dogbones maintaining ASTM D638-V. ATR-FTIR was performed with a ThermoScientific Nicolet iS10 at 25 °C. Differential scanning calorimetry (DSC) was conducted with a TA Instruments DSC 2500 was performed using heat/cool/heat cycles at 10 °C/min reporting 2nd heats. Number-average (M_n) and weight-average (M_w) molecular weight and dispersity ($Đ = M_w/M_n$) were determined from size exclusion chromatography (SEC) carried out on a Waters Alliance e2695 separation module outfitted with two Shodex KD-806 M columns in series 8 x 300 mm. Tetrahydrofuran at 1 mL/min was used as eluent maintaining 35 °C with sample injection volumes of 100 µL. Polystyrene standards were employed for SEC calibration. Analyte concentrations of 3 mg/mL were filtered through Teflon® membranes with 450 µm pores before injection. Small- and wide-angle X-ray scattering (SAXS/WAXS) was carried out on a XUESS 2.0 by Xenocs in the University of Pennsylvania's DEXS facility. All scattering data contains a combination of SAXS and WAXS data obtained from multiple sample-to-detector distances (SDs). The DEXS facility is equipped with a PILATUS 1 M detector for small-angle scattering, a PILATUS 100 K detector for wide-angle scattering, and a GeniX3D beam source (8 keV, Cu Kα, $\lambda = 1.54$ Å). All samples were sealed in 1.0 mm diameter glass capillaries. SAXS collection times were 30 min in high-resolution collimation with SDs of 363-6390 mm. WAXS collection times were 30 min in high-resolution collimation with an SD of 155 mm. The scattering data was integrated into I(q) plots. Small- and wide-angle data were arbitrarily shifted in I(q) plots.

2.4. Preparation of Photocast Films for Tensile Analysis and DMA

Photocured latex was prepared as described above. 3 g of each photocurable latex composition was placed in a 75 mm diameter Teflon® dish and irradiated for 30 s with an Omnicure S2000 high-pressure mercury light source. The films were subsequently air-dried for 18 h to ensure the absence of bubbles. The films were dried *in vacuo* at 120 °C for 20 min. Tensile dogbones were cut from dried films using a Pioneer-Dietecs ASTM D-638-V die and analyzed directly. Rectangular DMA specimens were cut from the photocast film and analyzed directly.

2.5. Preparation of Samples for Small- and Wide-Angle X-ray Scattering

Photocured latex was prepared as described above. A photorheometer with a 500 μm gap was used to generate photocured cast films maintaining consistent sample dimensions. Similarly, 3D printed cylinders with a diameter of 1 mm and a length of 5 mm were generated. Each sample was annealed for 20 min at 120 °C before testing.

2.6. Vat Photopolymerization of Latex

2.6.1. EnvisionTEC EnvisionOne DLP Printer

An EnvisionTEC Envision One continuous digital light manufacturing (cDLM) printer with oxygen inhibition build window technology was used to fabricate three-dimensional parts. The optical engine utilizes a 385 nm UV source and a digital light processing (DLP) unit featuring a 1920x1080 micromirror array in an orthogonal array orientation. A native 93 μm pixel resolution in the X-Y plane and Z-axis layer thickness of 100 μm with 1 s exposure time per layer was used.

2.6.2. Asiga MAX X27 DLP Printer

An Asiga MAX X27 DLP vat photopolymerization system was also used to fabricate three-dimensional parts. The standard build volume is 51.8 x 29.2 x 75 mm and uses a 385 nm high power UV LED to selectively cure with a 27 μm pixel resolution. Systematic determination of printing parameters was based on the adhesion of printed objects to the build platform, XY resolution, and absence of layer lines when observed under scanning electron microscopy (SEM). For 3D printed tensile specimens, 20 mm cubes, and octet/gyroid lattices a burn-in exposure time of 0.45 s per layer for 5 layers and a standard exposure time of 0.38 s per layer with an intensity of 21 mW/cm^2 was used. The Z-axis layer thickness was 45 µm, with submergence and withdrawal velocities of 2000 µm/s and 450 µm/s, respectively.

2.6.3. Post-Processing of 3D Printed Objects

3D printed specimens were transferred onto Teflon® dishes and allowed to air dry for 18 h. Subsequently, the Teflon® dishes containing the printed objects were placed in a vacuum oven preheated to 120 °C to anneal. The objects were held at 30 mmHg for 20 min. 20 min was determined with SAXS analysis to be sufficient at reaching a stable nanoscale morphology as described later. The pressure inside the vacuum oven was then quickly equilibrated. Dried parts were removed from the vacuum oven for further analysis.

3.0 Results & Discussion:

3.0.1 Compositional Design of Photocurable Polymer Latex:

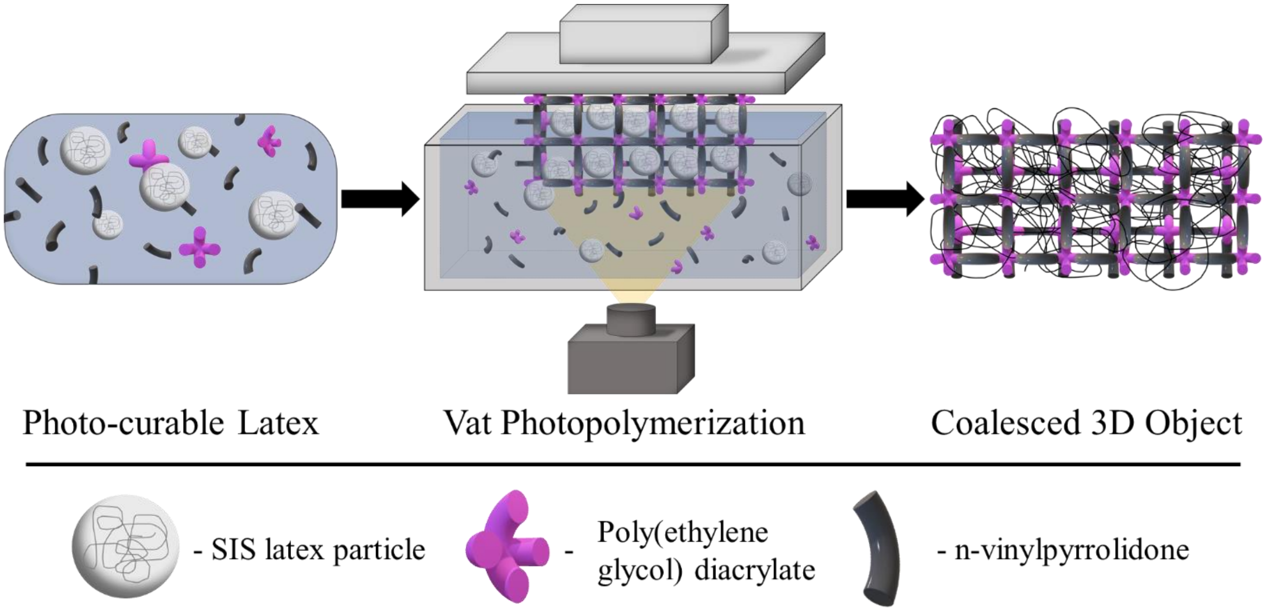

Figure 1. Vat photopolymerization 3D printing and subsequent post-printing processing of photocurable SIS latex to form interpenetrating polymer networks (IPN).

Figure 1 illustrates VPP of photocurable polymeric latex to print high molecular weight ABA SIS triblock copolymers. Addition of network precursors and photoinitiator to the aqueous phase enabled photopolymerization of the supporting scaffold. Iterative UV irradiation initiated free radical copolymerization of n-vinylpyrrolidone and poly(ethylene glycol) diacrylate resulting in a crosslinked scaffold embedded with high molecular weight triblock copolymer nanoparticles. Subsequent thermal post-processing volatilized water and promoted coalescence of dispersed nanoparticles throughout the photogenerated scaffold forming an interpenetrating network (IPN). The resulting IPN consisted of two distinct networks: (i) a photo-crosslinked scaffold network, which provided structural integrity throughout the printing process and served as a template for a 3D object, and (ii) a nanoscale phase separated ABA triblock copolymer physical network dictating mechanical performance of the 3D printed object. This latex printing platform is suitable for a variety of elastomeric latexes; however, SIS is the first example of an ABA triblock copolymer for VPP. SIS comprises a high T_g “hard” phase and a low T_g “soft” phase of polystyrene and polyisoprene, respectively, resulting in nanoscale phase separation within the covalently crosslinked network. Phase separation affords excellent elastomeric mechanical performance.

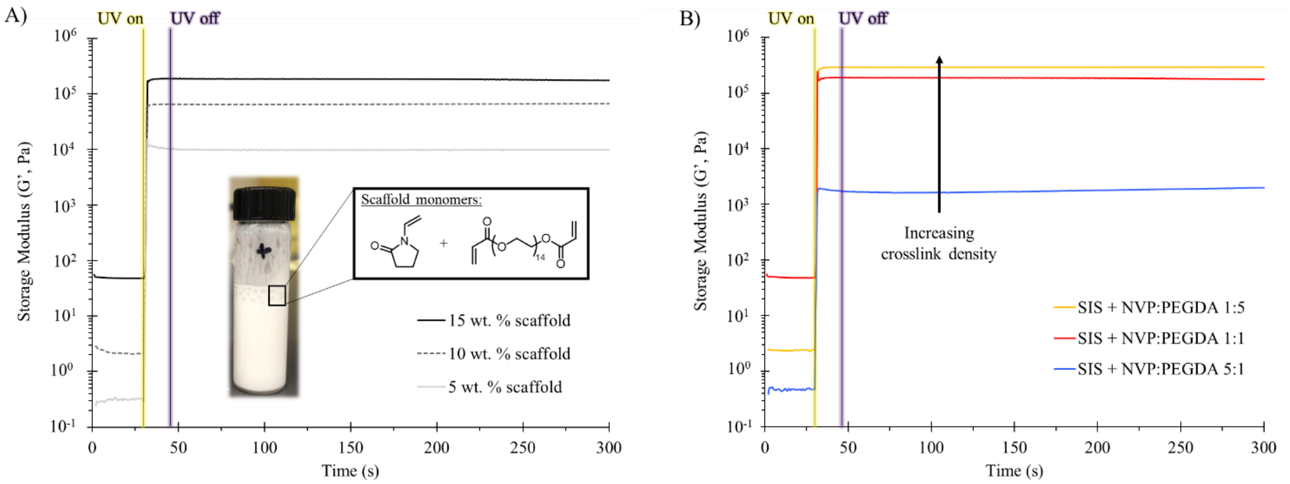

Figure 2. Photorheology of photocurable SIS latex with (A) increasing scaffold (NVP:PEGDA 1:1) content at identical compositions to determine optimal scaffold loading for VPP and (B) varying ratios of scaffold monomer and oligomer maintaining 15 wt. % scaffold to elucidate printability of scaffold compositions for VPP. Photorheology performed at 25 °C in air at 1 Hz

The scaffold composition addressed three key objectives: (i) ensuring scaffold monomers, oligomers, and photoinitiators did not compromise latex stability, (ii) achieving rapid scaffold generation with a modulus sufficient for the green body to withstanding the printing process, and (iii) ensuring the resulting scaffold imparted minimal decrease in mechanical performance. These criteria were essential for enabling high molecular weight AM latexes for producing mechanically robust complex geometries. The combination of NVP and PEGDA served as suitable scaffold precursors and enabled VPP of SIS triblock copolymer latex. Photorheological measurements guided the design of photoreactive latex compositions, revealing cure kinetics and storage modulus upon UV irradiation. The crossover time, which indicates the point at which the storage modulus exceeds the loss modulus (G'>G''), provided insight into photochemical reaction kinetics during UV exposure.[36] For samples containing 5-15 wt. % scaffold precursors

(NVP:PEGDA 1:1), crossover times were ~1 s, which indicated rapid network formation. Plateau shear storage moduli (G_N^0) corresponded to the M_c of the photo-crosslinked network, which was indicative of structural rigidity of the resulting green body.[6, 37, 38] Compositions containing 5, 10, and 15 wt. % scaffold exhibited G_N^0 values of 10000, 68000, and 175000 Pa, respectively, which indicated that compositions containing 10-15 wt. % scaffold precursors were suitable for 3D printing (**Figure 2**).

Varying scaffold precursor ratios enabled optimization for both printing (achieving higher G_N^0 for structural support) and enhanced mechanical performance (attaining lower G_N^0 resulting from increased M_c providing improved tensile performance). G_N^0 decreased significantly from 274000 to 3000 Pa with increased concentration of NVP (NVP:PEGDA 5:1) resulting from higher M_c. Compositions containing scaffold precursors NVP:PEGDA 1:1 provided ideal G_N^0 rapidly achieving 10^5 Pa·s. However, the influence of M_c on elastomer performance suggested scaffold composition NVP:PEGDA 5:1 was preferred despite achieving a storage modulus of 10^3 Pa·s. DLS confirmed the addition of scaffold precursors did not adversely affect the SIS particle size or particle size distribution, maintaining a hydrodynamic radius of 660 nm (**Figure 3**). For these reasons, compositions containing NVP:PEGDA 1:1 and 5:1 were further probed.

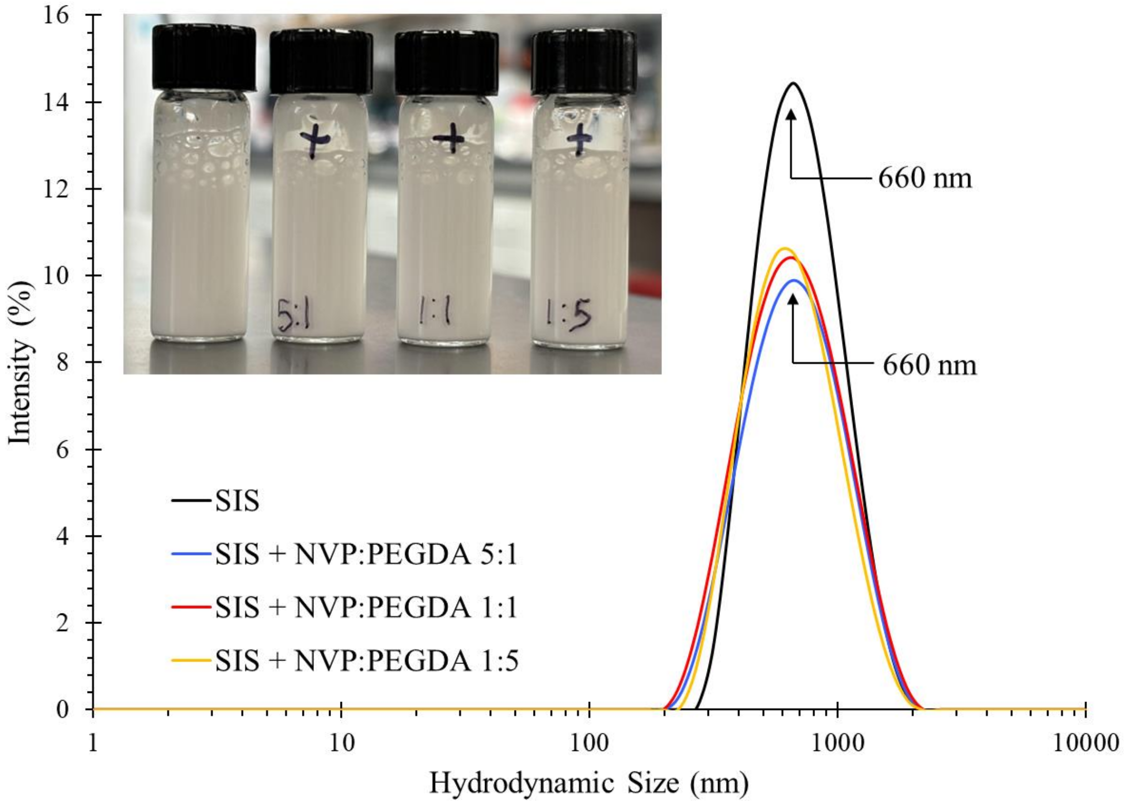

Figure 3. DLS measurements of neat SIS latex and 15 wt. % of each scaffold composition demonstrating photocurable latex stability after scaffold addition. Analyses conducted at 1 wt. % solids in deionized water at 25 °C

Thermal post-processing enhanced mechanical performance of printed structures by removing water and promoting polymer particle coalescence. Drying photocured green bodies *in vacuo* transformed the film from opaque to translucent, suggesting particle coalescence due to the disappearance of light-scattering phases. The resulting IPNs exhibited significantly improved mechanical performance compared to the green body precursors. Additionally, scaffold composition exhibited a significant impact on tensile behavior. Specifically, IPN films with increased PEGDA content (NVP:PEGDA 1:5) demonstrated failure at ~170% elongation (**Figure S3**), while cast films with higher NVP concentrations (NVP:PEGDA 5:1) exhibited an impressive 1200% elongation at break. This significant difference in mechanical performance was attributed to increased M_c for samples containing the NVP:PEGDA 5:1 scaffold, facilitating efficient particle coalescence. DMA revealed distinct T_g's, indicative of microphase separation. The polyisoprene T_g was observed at -46 °C, while the PEGDA:NVP scaffold T_g varied depending on composition (**Figure S4**). Interestingly, SIS NVP:PEGDA 5:1 specimen demonstrated a higher rubbery plateau modulus, despite having the highest M_c, suggesting enhanced polymer particle coalescence throughout the photogenerated scaffold. Broad thermal transitions for the polystyrene phase were observed; however, the loss of physical crosslinks resulted in film failure. 20 min annealing times demonstrated T_g shifts of the scaffold, indicating improved microphase separation (**Figure S5**). However, prolonged annealing led to a diminished scaffold T_g's suggesting microphase mixing. Furthermore, prolonged annealing led to increased variation in mechanical performance presumably due to a combination of thermoxidative crosslinking and microphase mixing (**Table S1)**. 20 min annealing at 120 °C *in vacuo* proved to be optimum, maintaining a balance between enhanced mechanical performance and minimal crosslinking. This annealing condition was applied for all subsequent sample preparation.

3.0.2 VPP of Photocurable SIS Polymer Latex:

Our previous research demonstrated a platform to enable the top-down VPP 3D printing of high molecular weight aqueous colloidal polymers, facilitating the production of high-performance elastomers. However, the presence of colloidal particles resulted in light scattering, thus reducing the average intensity of patterned UV light and diminishing feature fidelity and surface finish of the final printed object. Light scattering mitigation in SBR photocurable latex compositions necessitated (i) imaging of the scattered intensity distribution on the resin surface, (ii) predicting cured feature dimensions, and (iii) subsequent generation of corrected printing parameters. *In-situ* optical imaging, combined with a computer-vision algorithm provided feedback to guide the determination of printing parameters to compensate for light scattering, and enabled precise control of delivered UV irradiation. The vision-assisted printing algorithm successfully mitigated light scattering resulting in optimal feature fidelity and surface finish. However, reliance on specifically designed VPP systems equipped with computer-vision technology limited photocurable latexes to custom 3D printers.

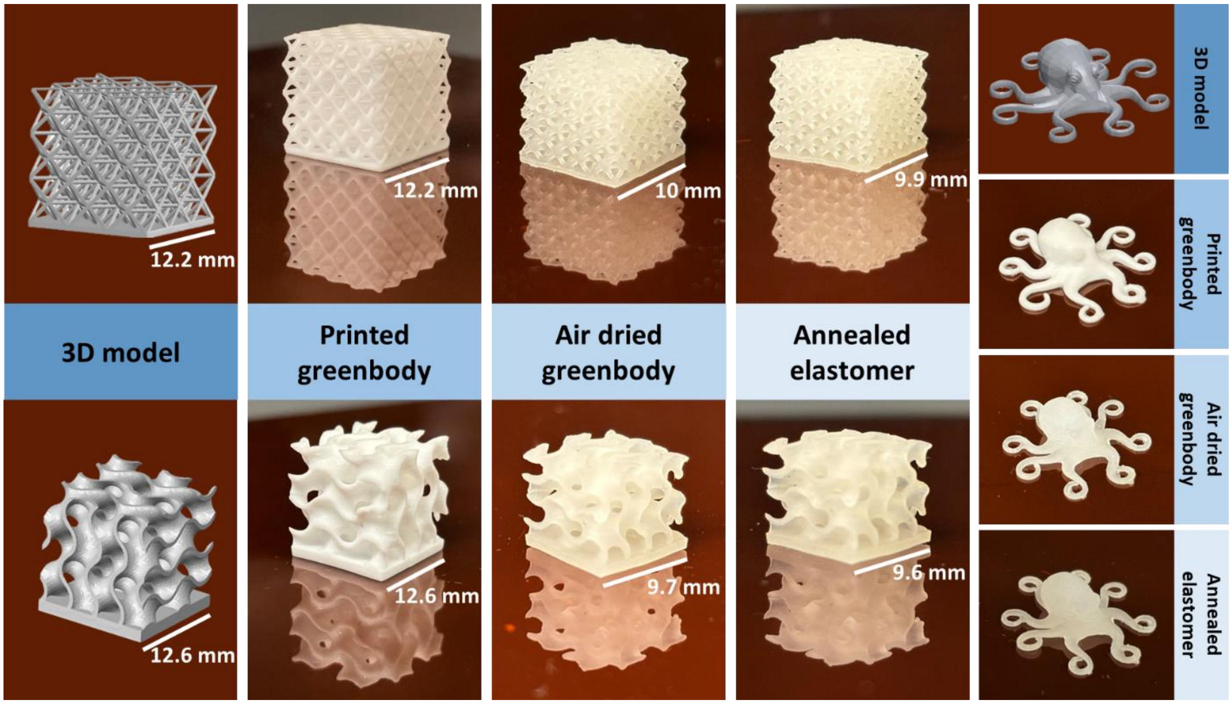

Figure 4. Evaluation of 3D objects printed from photocurable SIS NVP:PEGDA 5:1 depicting the achievable resolution and subsequent post-processing

To avoid the necessity of machine vision with our earlier custom printers, commercially available bottom-up 3D printers enabled photocurable latex compositions without computer-vision-based algorithms. Using bottom-up VPP systems that feature a membrane designed for oxygen inhibition of reaction reduced the XY overcuring that occurred due to light scattering in the top-down VPP systems. The use of bottom-up VPP systems thus enabled fabrication of 3D objects without specialized curing compensation software, while maintaining feature fidelity.

Increased crosslink density (higher PEGDA concentrations) enabled VPP of photocurable SIS. As expected, the increased crosslink density diminished mechanical performance resulting in relatively brittle parts. In contrast, the lowest crosslink density (NVP:PEGDA 5:1) demonstrated G_N^0 of 10^3 Pa, which is below the benchmark of 10^5 Pa for desired green body modulus. Successful 3D printing of photocurable SIS NVP:PEGDA 1:1 was initially chosen to enable refinement of printing parameter for photocurable SIS NVP:PEGDA 5:1 (**Figure S6, S7**). As expected, shifting to scaffold NVP:PEGDA 5:1 with printing parameters based on NVP:PEGDA 1:1 exhibited diminished XY resolution and printed object integrity. This discrepancy in resolution and integrity was attributed to differing relative reactivities of NVP to PEGDA leading to lower G_N^0 resulting from increased M_c (**Figure S8**). Lower G_N^0 suggested a mechanically poor scaffold, indicating minimal required force to damage intricate features. Adjustments in withdrawal and approach velocity of the build platform were made to minimize the applied force and subsequent deformation during submergence/withdrawal steps in the printing process. Exposure times and intensity were systematically tuned to achieve balance between XY resolution, part integrity, and mechanical performance, ultimately enabling successful printing of photocurable SIS NVP:PEGDA 5:1 (**Figure 4**). This demonstrated the capability to print exceptionally soft materials.

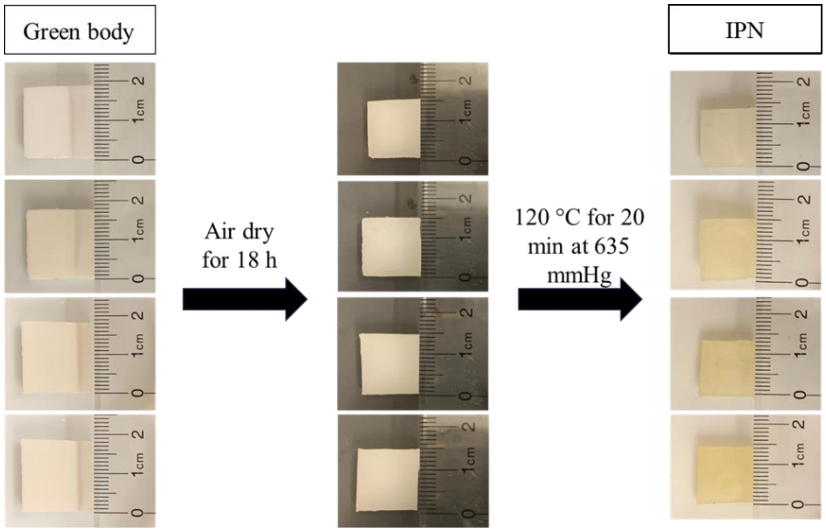

Direction	Average Air Dry Shrinkage (%)	Average Annealing Shrinkage (%)
X	21 ± 0.7	3 ± 0.7
Y	21 ± 0.5	4 ± 0.7
Z	23 ± 1.3	1 ± 0.5
Total Volumetric Shrinkage = 55.9 %		

Figure 5. VPP printed cubes from photocurable SIS containing 15 wt. % scaffold (NVP:PEGDA 5:1) for shrinkage analysis. Depicting green bodies directly after printing (left), air dried green bodies (middle), and annealed IPNs (right) with tabulated average shrinkage values (bottom).

Thermal post-processing of 3D printed SIS NVP:PEGDA 5:1 green bodies to produce IPNs resulted in the loss of a substantial volume fraction of water (~50 vol%), corresponding to the observed nearly isotropic volumetric shrinkage of approximately 55 vol % (dimensional shrinkage of ~22%), as depicted in **Figure 5**. Following the established drying and annealing procedure, printed objects underwent a gradual drying process on a Teflon® dish, which preserved the structural fidelity of intricate features. The resulting dry IPN parts exhibited varying degrees of translucency depending upon geometry thickness. Literature suggested the absence of discrete interfaces between layers provides optical clarity.[39] However, photocurable

SIS compositions exhibited opaque appearances irrespective of printing parameters or post-processing procedures. This physical characteristic was attributed to the IPN morphology and chemical dissimilarity.

3.0.3 Evaluation of Morphology and Elastic Performance of Printed Elastomers:

Block copolymers exhibit unique behavior enabling diverse applications in material science. Comprised of two or more chemically distinct polymer segments covalently bound together, the material properties of block copolymers result from microphase separation. This inherent immiscibility results in segregation of each block creating nanoscale domains of distinct chemical composition and various shapes.[39] The microphase separation of block copolymers is a critical aspect of their functionality that leads to distinct physical and chemical properties. SIS relies heavily on microphase separation with a high T_g “rigid” polystyrene phase forming physical crosslinks and a “soft” low T_g polyisoprene phase providing elasticity. The synergy of these two phases provides SIS with a balance of strength and elasticity resulting in excellent mechanical performance. However, the incorporation of a scaffold that is required for VPP potentially hinders microphase separation leading to less ordered domains resulting in a turbid or opaque appearance. Furthermore, the introduction of a polymer scaffold exemplifies the chemical dissimilarity, contributing to the observed visual opacity.

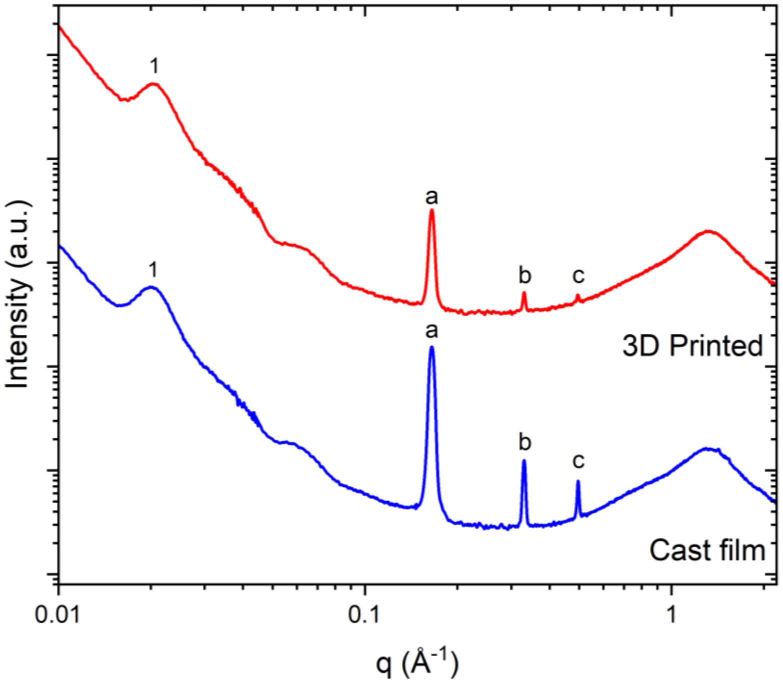

Figure 6. 1D profile of azimuthally integrated 2D patterns of photocurable SIS (NVP:PEGDA 5:1). Both the 3D printed and cast films exhibit microphase separated domains without long-range order (peak 1), as well as crystalline SDS (peaks a, b, c).

X-ray scattering of photocured cast films and 3D printed objects revealed nearly identical X-ray scattering patterns, suggesting comparable morphologies (**Figure 6**). Specifically, a peak at ~0.02 Å^{-1} and its adjacent shoulder are indicative of liquidlike packing of spherical domains of polystyrene with an average center-to-center distance of 300 Å. The X-ray scattering data of neat SIS have a similar peak and shoulder, indicating that the presence of the scaffold has minimal effect on the morphology of the SIS triblock copolymer (**Figure S9**). Prolonged post-processing extending the 120 °C annealing from 20 min to 36 h showed an insignificant effect on the final morphology for either cast films or 3D printed objects (**Figure S10**). Note that the sharp peaks labeled a, b, and c have a ratio (q_i/q_1) of 1:2:3, which is characteristic of a layered structure. These scattering features are consistent with SDS crystals.[40] This finding suggests an excess of SDS within the composition; however, attempts to reduce the surfactant concentration resulted in photocurable composition instability (**Figure S11)**. Furthermore, post-processing increased the relative SDS concentration within a chemically dissimilar matrix driving crystallization. While SDS crystals remain too small to scatter light, the chemical interfacial dissimilarity between scaffold, SIS, and SDS crystals presumably induces refractive index (RI) changes, which causes opacity. The X-ray scattering demonstrates the presence of nominally spherical microphase separated domains and provides evidence of block copolymer latexes functioning within VPP. Furthermore, preliminary TEM analysis indicated the presence of a low level of triblock copolymer aggregates despite leveraging optimal annealing conditions providing pathways for further improvement of mechanical performance. Future studies will probe the role of crosslink density of the scaffold, annealing conditions, and scaffold composition. Despite the presence of residual nanoparticle aggregates, tensile performance was reproducible. Despite constraints imposed by the added photocurable scaffold, this morphological analysis adds a significant dimension to the understanding of photocurable latexes for VPP.

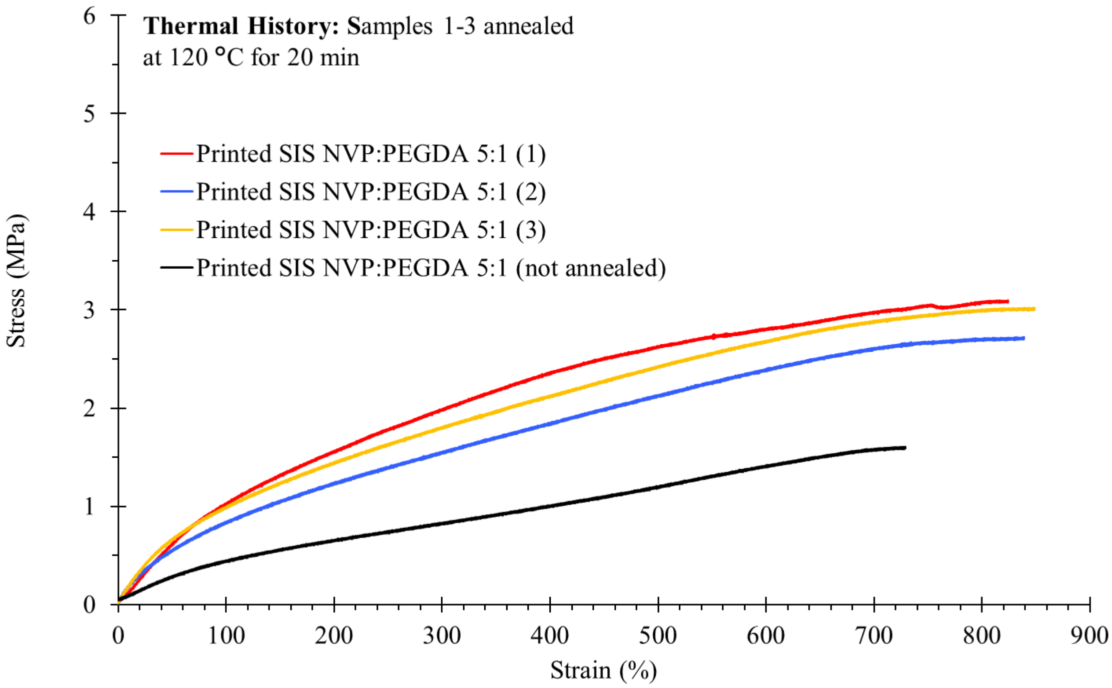

Figure 7. Tensile analysis of VPP printed tensile specimens (NVP:PEGDA 5:1) confirming consistent tensile behavior between multiple specimens with all achieving extensibility above 800%. Tensile testing was conducted in air at 25 °C

3D printed tensile specimen (modified ASTM D-638 IV) exhibited remarkable elongations of 847±12% with an ultimate stress of 3.0±0.2 MPa (**Figure 7**), which to the best of our knowledge, represents the first VPP example of ABA triblock copolymer elastomers. Furthermore, scaffold variability enabled precise control of 3D printed object moduli. Moreover, hysteresis analysis for SIS NVP:PEGDA 5:1 was evaluated at 500% elongation for 5 cycles (**Figure 8**). After the first cycle, samples exhibited a marginal loss of ~30 % and 0.5 MPa, demonstrating minimal deviation in mechanical performance for subsequent cycles. These results aligned with our previous work involving SBR.[34] This observed reduction in mechanical performance was attributed to elongation exceeding the scaffold's capabilities despite its compositional design to provide higher M_c. However, the test specimen maintained structural fidelity beyond the yield point of the scaffold, underlining the robustness of the developed 3D printed elastomers.

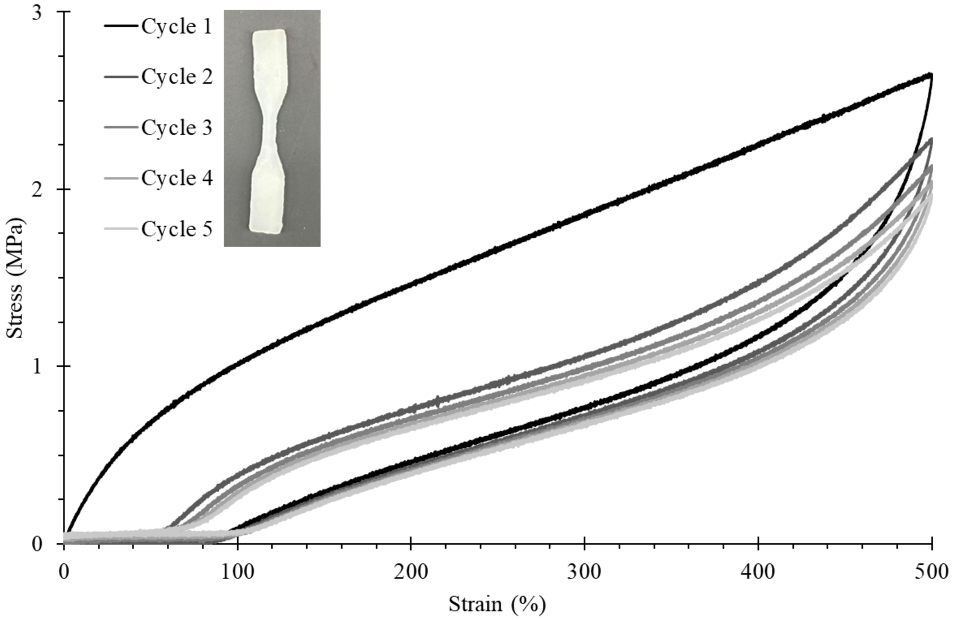

Figure 8. Cyclic tensile testing of 3D printed SIS latex with NVP:PEGDA 5:1 scaffold reaching 500% elongation for each cycle. Tensile testing was conducted in air at 25 °C

4. Conclusions

Navigating the intricate balance between printed object resolution, integrity, and subsequent mechanical performance remains a challenging paradox for photocurable high molecular weight polymers in VPP. Polymeric latexes provide a path to printing high molecular weight materials while maintaining viscosities conducive to VPP. Additionally, the unique advantage of 3D printing from aqueous systems enables a platform for fabrication of high performance IPN elastomers without organic solvents. Our investigation demonstrated the extension of VPP 3D printing to high molecular weight ABA triblock copolymers. X-ray scattering revealed the nanoscale phase separation of the interpenetrating ABA triblock copolymer providing the physical crosslink determinant for optimal mechanical performance. Implementation of a low modulus scaffold composition was established on commercially available bottom-up VPP systems. This work expands the opportunities for VPP printing of elastomers but also demonstrates the first successful implementation of ABA triblock copolymers for VPP. The achieved tensile performance exceeds 800% elongation and demonstrated elasticity maintain mechanical performance after cyclic testing.

Acknowledgements:

This research was supported in part from the REMADE national institute, project 20-01-RM-4007. Margaret K. Brown and Karen I. Winey acknowledge funding from NSF-DMR-1904767 and the use of the Dual-source Environmental X-ray Scattering (DEXS) facility supported by the Laboratory for Research on the Structure of Matter at the University of Pennsylvania Materials Research Science and Engineering Center (MRSEC) DMR-2309043.

Supporting Info

Vat Photopolymerization 3D Printing of ABA Poly(styrene-*b*-isoprene-*b*-styrene) Triblock Copolymers

Ren H. Bean[1], Garvit Nayyar[1], Margaret K. Brown[3], Jianheng Wen[1], Yiqun Fu[2], Karen I. Winey[3], Christopher B. Williams[2], and Timothy E. Long[1*]

[1]School of Molecular Sciences & Biodesign Center for Sustainable Macromolecular Materials & Manufacturing (SM3), Arizona State University, Tempe, AZ 85281
[2]Department of Mechanical Engineering, Macromolecules Innovation Institute, Virginia Tech, Blacksburg, VA 24061
[3]Department of Materials Science and Engineering, University of Pennsylvania, Philadelphia, PA 19104

*To whom correspondence should be addressed. Email: telong@asu.edu. TEL: (480) 965-9539

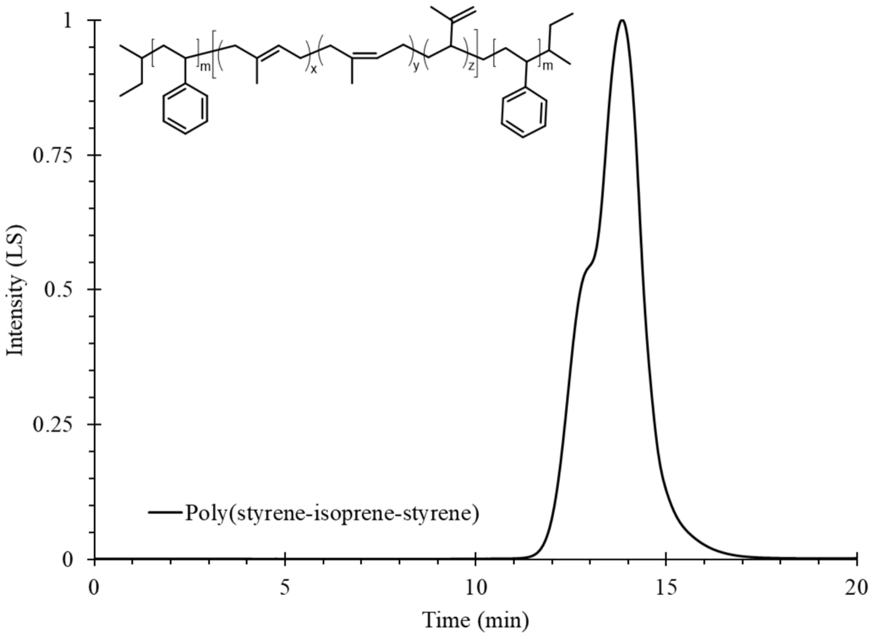

Figure S1. SEC affords molecular weight distribution of neat SIS. SEC was performed in THF at 23 °C

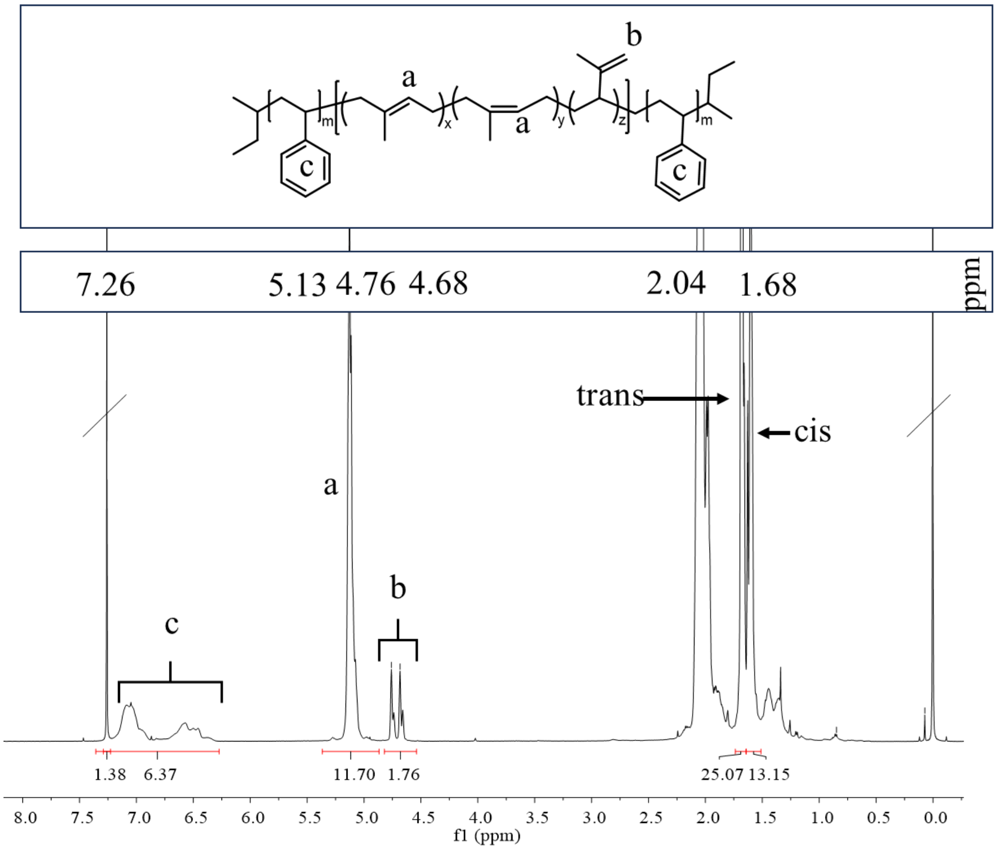

Figure S2. ^{1}H NMR spectrum of neat SIS. Spectroscopy performed in $CDCl_3$

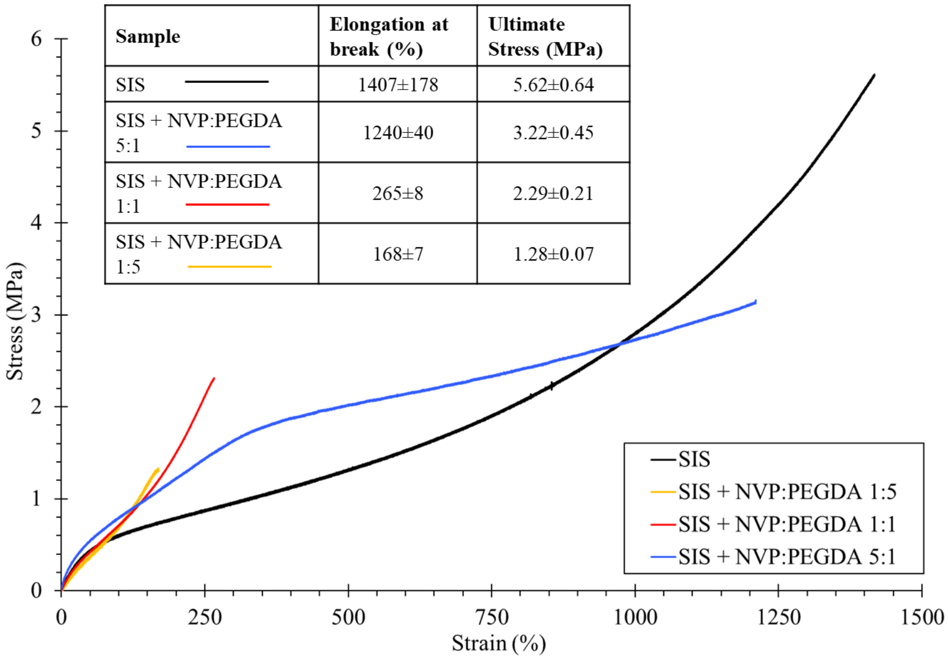

Sample	Elongation at break (%)	Ultimate Stress (MPa)
SIS	1407±178	5.62±0.64
SIS + NVP:PEGDA 5:1	1240±40	3.22±0.45
SIS + NVP:PEGDA 1:1	265±8	2.29±0.21
SIS + NVP:PEGDA 1:5	168±7	1.28±0.07

Figure S3. Tensile performance of photocured SIS latex with varying scaffold compositions while maintaining 15 wt. % scaffold. Tensile performed at 25 °C in air

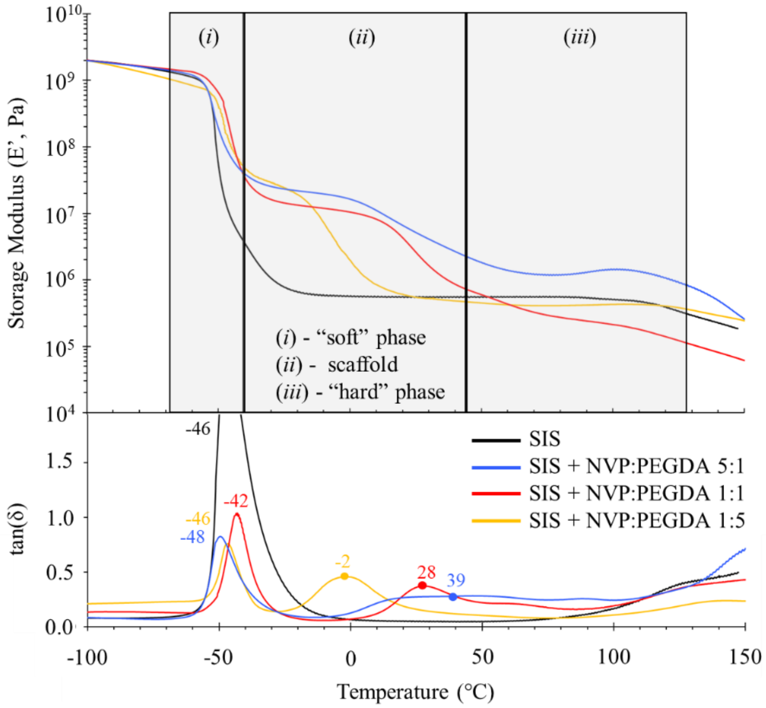

Figure S4. DMA of photocured SIS latex with varying ratios of scaffold molecules maintaining 15 wt. % scaffold and an annealing time of 20 min at 120 °C. Testing performed at 0.2% strain

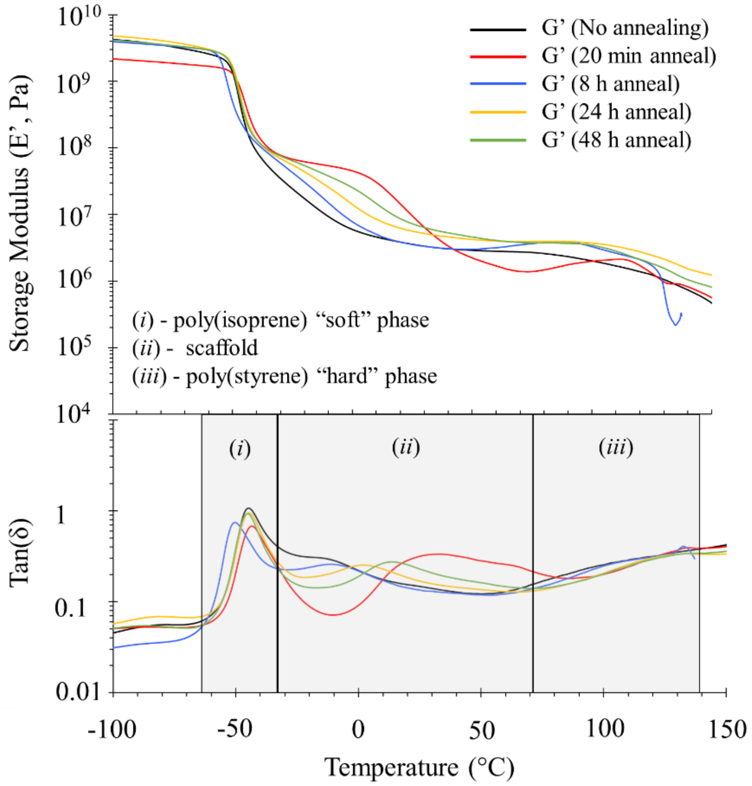

Figure S5. DMA of photocured SIS NVP:PEGDA 5:1 latex with varied annealing times demonstrating improved microphase separation with 20 min annealing and microphase mixing with extended annealing. Testing performed at 0.2% strain

Table S1. Tensile performance of photocured cast films of SIS latex with NVP:PEGDA 5:1 varying annealing times to test particle coalescence. Tests conducted in air at 25 °C

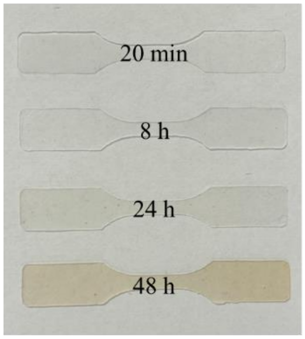

Annealing Time	Average Elongation at Break (%)	Average Ultimate Stress (MPa)	Average Youngs Modulus (MPa)
20 min	1260 ± 40	2.75 ± 0.34	0.84 ± 0.17
8 h	1280 ± 72	2.08 ± 0.15	1.29 ± 0.03
24 h	1293 ± 175	2.85 ± 0.50	1.35 ± 0.21
48 h	1247 ± 216	2.61 ± 0.30	1.31 ± 0.24

*All samples contain scaffold NVP:PEGDA 5:1

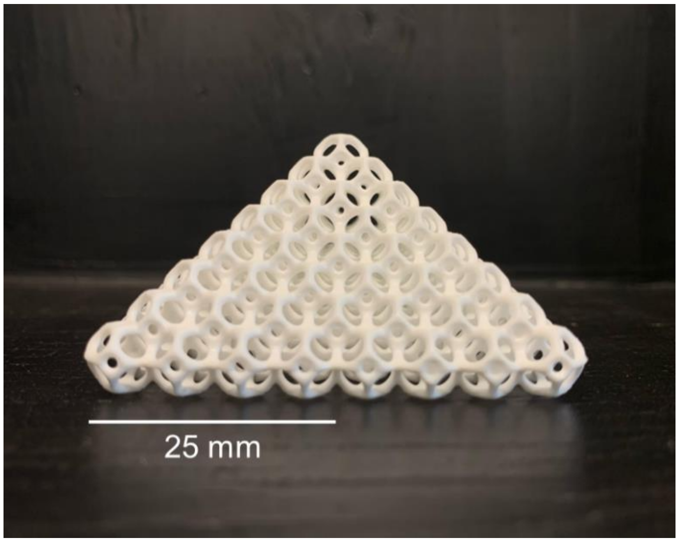

Figure S6. Evaluation of 3D lattice printed from SIS NVP:PEGDA 1:1 composition demonstrating achievable geometric complexity and composition variability. Depicted object has a strut size of 800 µm and was fabricated on an EnvisionOne cDLP system.

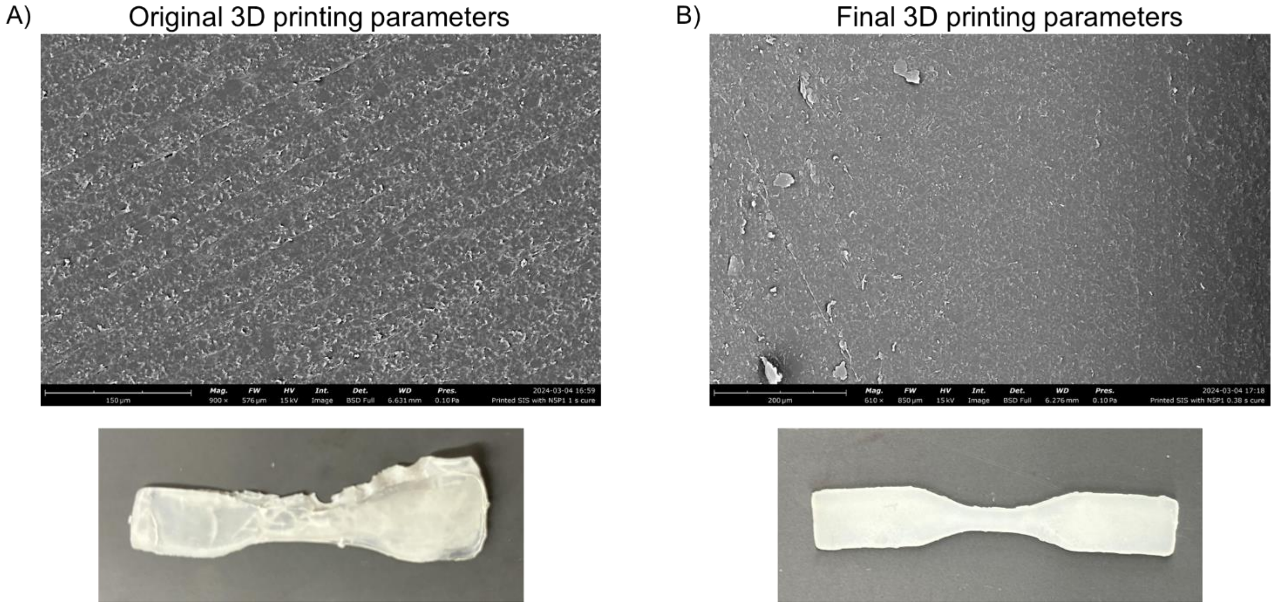

Figure S7. Scanning electron microscopy (SEM) of 3D printed SIS + NVP:PEGDA 5:1 demonstrating (A) original printing parameters from SIS + NVP:PEGDA 1:1 compositions and (B) final 3D printing parameters

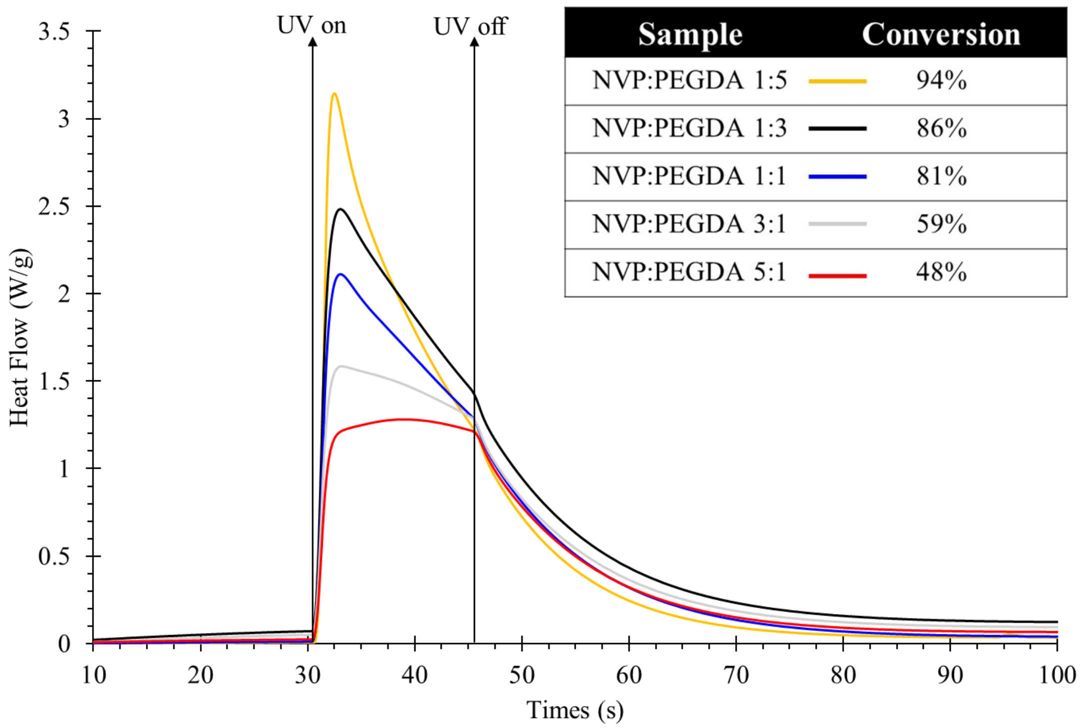

Figure S8. Photo-differential scanning calorimetry of photocurable SIS compositions demonstrating the reduced conversion with increasing NVP concentrations.

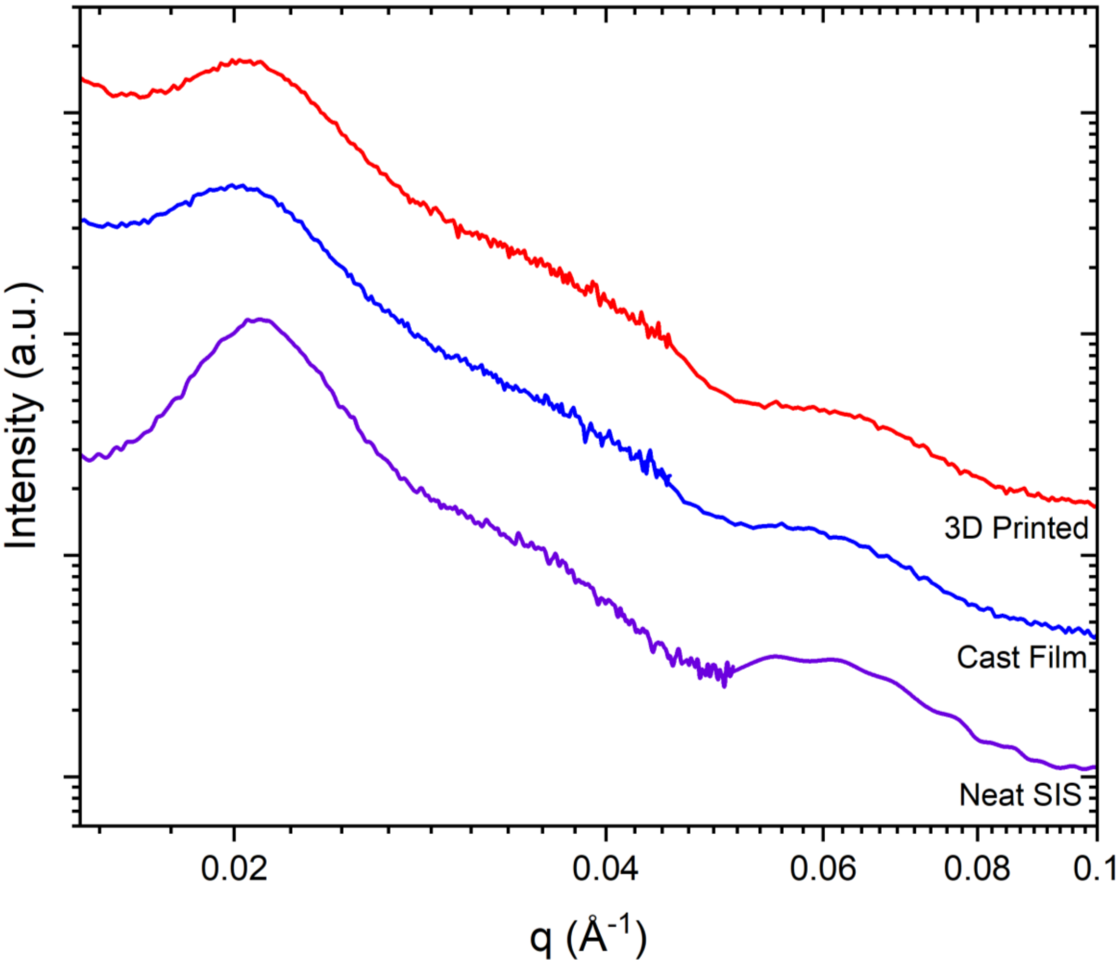

Figure S9. 1D profile of azimuthally integrated 2D X-ray scattering patterns of 3D printed and cast film photocured SIS (NVP:PEGDA 5:1), and neat SIS. All materials exhibited microphase separated morphologies without long-range order consistent with liquid-like packing of spherical domains.

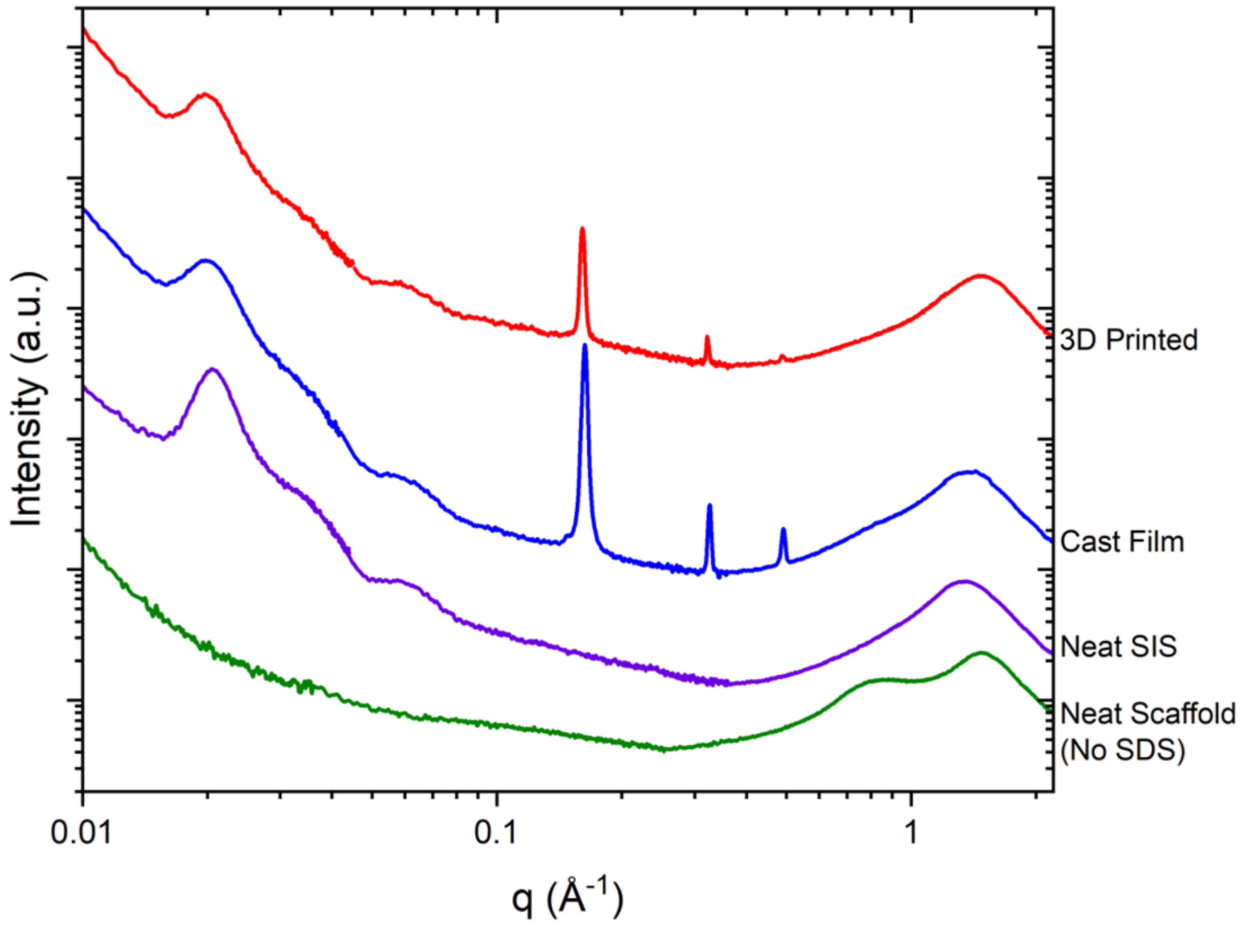

Figure S10. X-ray scattering profiles of photocured 3D printed and photocured cast films of SIS (NVP:PEGDA 5:1), neat SIS, and neat scaffold (omitting latex). All samples were post-processed at 120 °C for 36 h, which produces no morphological change.

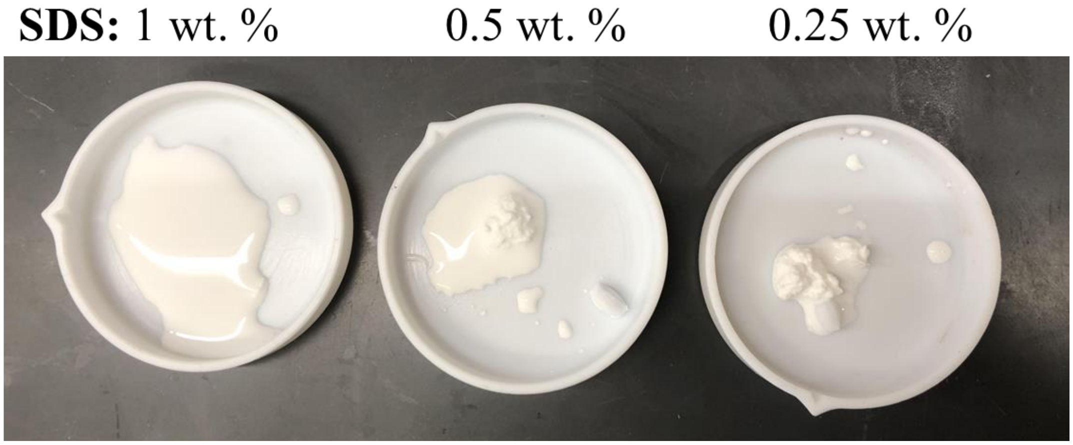

Figure S11. Analysis of varying SDS surfactant concentrations demonstrating latex instability with compositions containing less than 1 wt. %

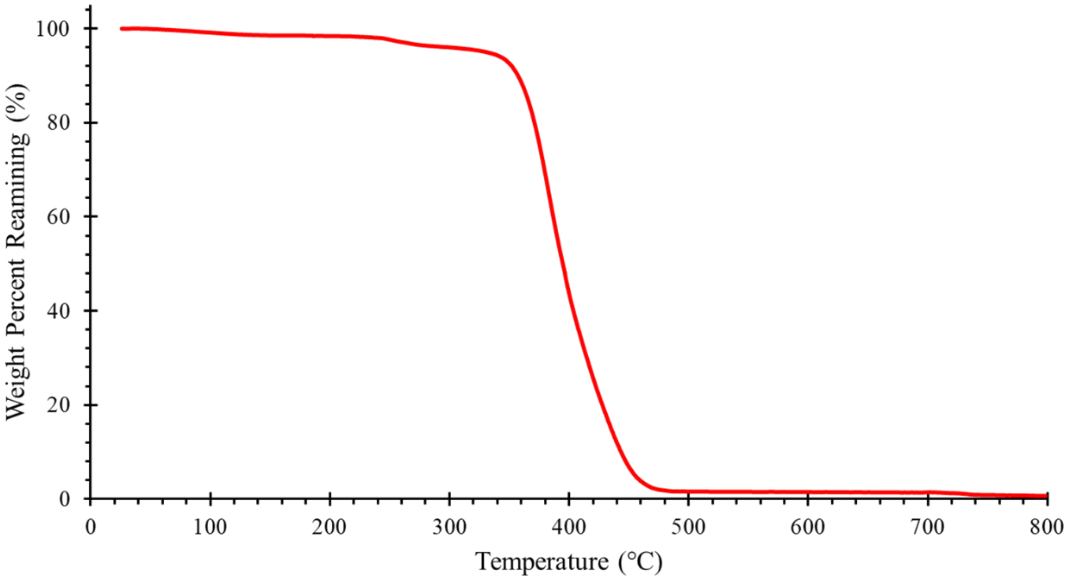

Figure S12. Thermogravimetric analysis indicates $T_{d,\,5\,\%}$ at 340 °C of the printed part after annealing at 120 °C for 20 min with absence of volatiles.

References:

1. Ngo, T. D.; Kashani, A.; Imbalzano, G.; Nguyen, K. T.; Hui, D., Additive manufacturing (3D printing): A review of materials, methods, applications and challenges. *Composites Part B: Engineering* **2018,** *143*, 172-196.
2. Jacobs, P. F., *Rapid Prototyping & Manufacturing: Fundamentals of Stereolithography*. Society of Manufacturing Engineers: 1992.
3. Schüller-Ravoo, S.; Teixeira, S. M.; Feijen, J.; Grijpma, D. W.; Poot, A. A., Flexible and Elastic Scaffolds for Cartilage Tissue Engineering Prepared by Stereolithography Using Poly(trimethylene carbonate)-Based Resins. *Macromolecular Bioscience* **2013,** *13* (12), 1711-1719.
4. Mondschein, R. J.; Kanitkar, A.; Williams, C. B.; Verbridge, S. S.; Long, T. E., Polymer structure-property requirements for stereolithographic 3D printing of soft tissue engineering scaffolds. *Biomaterials* **2017,** *140*, 170-188.
5. Kasprzak, C.; Brown, J. R.; Feller, K.; Scott, P. J.; Meenakshisundaram, V.; Williams, C.; Long, T., Vat Photopolymerization of Reinforced Styrene–Butadiene Elastomers: A Degradable Scaffold Approach. *ACS Applied Materials & Interfaces* **2022,** *14* (16), 18965-18973.

6. Bean, R. H.; Rau, D. A.; Williams, C. B.; Long, T. E., Rheology guiding the design and printability of aqueous colloidal composites for additive manufacturing. *Journal of Vinyl and Additive Technology* **2023,** *29* (4), 607-616.

7. Hegde, M.; Meenakshisundaram, V.; Chartrain, N.; Sekhar, S.; Tafti, D.; Williams, C. B.; Long, T. E., 3D printing all-aromatic polyimides using mask-projection stereolithography: processing the nonprocessable. *Advanced Materials* **2017,** *29* (31), 1701240.

8. Scott, P. J.; Meenakshisundaram, V.; Chartrain, N. A.; Sirrine, J. M.; Williams, C. B.; Long, T. E., Additive manufacturing of hydrocarbon elastomers via simultaneous chain extension and cross-linking of hydrogenated polybutadiene. *ACS Applied Polymer Materials* **2019,** *1* (4), 684-690.

9. Weyhrich, C. W.; Will, J. W.; Heifferon, K. V.; Brown, J. R.; Arrington, C. B.; Meenakshisundaram, V.; Williams, C. B.; Long, T. E., 3D-Printing of Poly(arylene ether sulfone)s: Functional High-Performance Polymers for Vat Photopolymerization. *Macromolecular Chemistry and Physics* **2023,** *224* (1), 2200240.

10. Sirrine, J. M.; Meenakshisundaram, V.; Moon, N. G.; Scott, P. J.; Mondschein, R. J.; Weiseman, T. F.; Williams, C. B.; Long, T. E., Functional siloxanes with photo-activated, simultaneous chain extension and crosslinking for lithography-based 3D printing. *Polymer* **2018,** *152*, 25-34.

11. Wilts, E. M.; Pekkanen, A. M.; White, B. T.; Meenakshisundaram, V.; Aduba, D. C.; Williams, C. B.; Long, T. E., Vat photopolymerization of charged monomers: 3D printing with supramolecular interactions. *Polymer Chemistry* **2019,** *10* (12), 1442-1451.

12. Derry, M. J.; Smith, T.; O'Hora, P. S.; Armes, S. P., Block Copolymer Nanoparticles Prepared via Polymerization-Induced Self-Assembly Provide Excellent Boundary Lubrication Performance for Next-Generation Ultralow-Viscosity Automotive Engine Oils. *ACS Applied Materials & Interfaces* **2019,** *11* (36), 33364-33369.

13. Gopalan, A. M.; Naskar, K., Ultra-high molecular weight styrenic block copolymer/TPU blends for automotive applications: Influence of various compatibilizers. *Polymers for Advanced Technologies* **2019,** *30* (3), 608-619.

14. Maji, P.; Naskar, K., Styrenic block copolymer-based thermoplastic elastomers in smart applications: Advances in synthesis, microstructure, and structure–property relationships—A review. *Journal of Applied Polymer Science* **2022,** *139* (39), e52942.

15. Bates, C. M.; Bates, F. S., 50th Anniversary Perspective: Block Polymers-Pure Potential. *Macromolecules* **2017,** *50* (1), 3-22.

16. Feng, H.; Lu, X.; Wang, W.; Kang, N.-G.; Mays, J. W., Block copolymers: Synthesis, self-assembly, and applications. *Polymers* **2017,** *9* (10), 494.

17. Jeong, B.; Bae, Y. H.; Lee, D. S.; Kim, S. W., Biodegradable block copolymers as injectable drug-delivery systems. *Nature* **1997,** *388* (6645), 860-862.

18. Kataoka, K.; Harada, A.; Nagasaki, Y., Block copolymer micelles for drug delivery: design, characterization and biological significance. *Advanced Drug Delivery Reviews* **2012,** *64*, 37-48.

19. Agrahari, V.; Agrahari, V., Advances and applications of block-copolymer-based nanoformulations. *Drug Discovery Today* **2018,** *23* (5), 1139-1151.

20. Hasannia, M.; Aliabadi, A.; Abnous, K.; Taghdisi, S. M.; Ramezani, M.; Alibolandi, M., Synthesis of block copolymers used in polymersome fabrication: Application in drug delivery. *Journal of Controlled Release* **2022,** *341*, 95-117.

21. Gaucher, G.; Dufresne, M.-H.; Sant, V. P.; Kang, N.; Maysinger, D.; Leroux, J.-C., Block copolymer micelles: preparation, characterization and application in drug delivery. *Journal of Controlled Release* **2005,** *109* (1-3), 169-188.

22. Park, T. H.; Eoh, H.; Jung, Y.; Lee, G.-W.; Lee, C. E.; Kang, H. S.; Lee, J.; Kim, K.-B.; Ryu, D. Y.; Yu, S.; Park, C., Thermo-Adaptive Block Copolymer Structural Color Electronics. *Advanced Functional Materials* **2021,** *31* (11), 2008548.

23. Ditte, K.; Perez, J.; Chae, S.; Hambsch, M.; Al-Hussein, M.; Komber, H.; Formanek, P.; Mannsfeld, S. C.; Fery, A.; Kiriy, A., Ultrasoft and high-mobility block copolymers for skin-compatible electronics. *Advanced Materials* **2021,** *33* (4), 2005416.

24. Blau, R.; Chen, A. X.; Polat, B.; Becerra, L. L.; Runser, R.; Zamanimeymian, B.; Choudhary, K.; Lipomi, D. J., Intrinsically stretchable block copolymer based on PEDOT: PSS for improved performance in bioelectronic applications. *ACS Applied Materials & Interfaces* **2022,** *14* (4), 4823-4835.

25. da Silva, C.; Budde, H.; Menzel, M.; Wendler, U.; Bartke, M.; Weydert, M.; Beiner, M., Self-assembled structure and relaxation dynamics of diblock copolymers made of polybutadiene and styrene/butadiene rubber. *RSC advances* **2016,** *6* (56), 50460-50470.

26. Matyjaszewski, K.; Gnanou, Y.; Leibler, L., *Macromolecular Engineering*. Wiley Online Library: 2011.

27. Bobrin, V. A.; Yao, Y.; Shi, X.; Xiu, Y.; Zhang, J.; Corrigan, N.; Boyer, C., Nano-to macro-scale control of 3D printed materials via polymerization induced microphase separation. *Nature Communications* **2022,** *13* (1), 3577.

28. Bobrin, V. A.; Lee, K.; Zhang, J.; Corrigan, N.; Boyer, C., Nanostructure Control in 3D Printed Materials. *Advanced Materials* **2022,** *34* (4), 2107643.

29. Goyal, S.; Yesu, A.; Banerjee, S. S., Direct ink writing-based additive manufacturing of styrene-isoprene-styrene block copolymer. *Polymer Engineering & Science* **2023,** *63* (11), 3708-3718.

30. Xie, R.; Mukherjee, S.; Levi, A. E.; Reynolds, V. G.; Wang, H.; Chabinyc, M. L.; Bates, C. M., Room temperature 3D printing of super-soft and solvent-free elastomers. *Science Advances* **2020,** *6* (46), eabc6900.

31. Seo, M.; Hillmyer, M. A., Reticulated nanoporous polymers by controlled polymerization-induced microphase separation. *Science* **2012,** *336* (6087), 1422-1425.

32. Lee, K.; Corrigan, N.; Boyer, C., Polymerization induced microphase separation for the fabrication of nanostructured materials. *Angewandte Chemie* **2023,** *135* (44), e202307329.

33. Oh, T.; Cho, S.; Yoo, C.; Yeo, W.; Oh, J.; Seo, M., Polymerization-Induced Microphase Separation of a Polymerization Mixture into Nanostructured Block Polymer Materials. *Progress in Polymer Science* **2023**, 101738.

34. Scott, P. J.; Meenakshisundaram, V.; Hegde, M.; Kasprzak, C. R.; Winkler, C. R.; Feller, K. D.; Williams, C. B.; Long, T. E., 3D printing latex: a route to complex geometries of high molecular weight polymers. *ACS Applied Materials & Interfaces* **2020,** *12* (9), 10918-10928.

35. Scott, P. J.; Rau, D. A.; Wen, J.; Nguyen, M.; Kasprzak, C. R.; Williams, C. B.; Long, T. E., Polymer-inorganic hybrid colloids for ultraviolet-assisted direct ink write of polymer nanocomposites. *Additive Manufacturing* **2020,** *35*, 101393.

36. Bean, R. H.; Rau, D. A.; Williams, C. B.; Long, T. E., Rheology guiding the design and printability of aqueous colloidal composites for additive manufacturing. *Journal of Vinyl and Additive Technology* **2023**.

37. Rubinstein, M., Polymer physics—The ugly duckling story: will polymer physics ever become a part of "proper" physics? *Journal of Polymer Science Part B: Polymer Physics* **2010,** *48* (24), 2548-2551.
38. Tianhong, T., Quantifying Polymer Crosslinking Density Using Rheology and DMA. *TA Instruments* **2020**, 2-4.
39. Dobson, A. L.; Huang, S.; Bowman, C. N., Modeling Phase Separation of Free-Radical Polymerizations in Crosslinked Networks. *Macromolecules* **2024**.
40. Dell, S. S., The crystal structure of sodium dodecylsulfate. *Acta Chem. Scand. A* **1977,** *31* (10).